Fuel 405 (2026) 136422

Contents lists available at ScienceDirect

Fuel

journal homepage: www.elsevier.com/locate/jfue

Full length article

Reduction of micron-sized iron oxide particles with high initial porosity in a fluidized bed reactor using hydrogen: Morphology and phase analysis

Malte Seitz[a], Martin P. Kannengießer[a], Björn Stelzner[a,*], Fabian P. Hagen[a], Lukas Braun[b,c], Jonas Kaltenbach[d], Kerstin Märkle[d], Martin Peterlechner[d], Jonas Spielmann[e], Dmitry E. Doronkin[b,c], Max P. Deutschmann[f], Jan-Dierk Grunwaldt[b,c], Yolita M. Eggeler[d], Ulrike I. Kramm[e], Hermann Nirschl[f], Dimosthenis Trimis[a]

[a] Karlsruhe Institute of Technology (KIT), Engler-Bunte-Institute, Combustion Technology, Karlsruhe, Germany
[b] Karlsruhe Institute of Technology (KIT), Institute for Chemical Technology and Polymer Chemistry, Karlsruhe, Germany
[c] Karlsruhe Institute of Technology (KIT), Institute of Catalysis Research and Technology, Eggenstein-Leopoldshafen, Germany
[d] Karlsruhe Institute of Technology (KIT), Laboratory for Electron Microscopy, Karlsruhe, Germany
[e] Technical University of Darmstadt, Catalysts and Electrocatalysts Group, Darmstadt, Germany
[f] Karlsruhe Institute of Technology (KIT), Institute of Mechanical Process Engineering and Mechanics, Karlsruhe, Germany

HIGHLIGHTS

- Reduction of generic iron(III)oxide particles with high porosity, with an initial morphology similar to that observed after multiple oxidation–reduction cycles, influences their reduction in a fluidized bed.
- Reduction Pathways: Two pathways were investigated: (1) Direct reduction of Fe_3O_4 to Fe and (2) Stepwise reduction via FeO.
- Morphological Changes During Reduction: Bimodal pore size shift: initial small pores decreased after reduction, while larger pores significantly increased.
- Measurement Techniques: TGA & calorimetry provided accurate reduction measurements, while XRD & Mössbauer Spectroscopy analyzed residual iron oxides.
- Surface Area Changes: The specific surface area decreased by ~15 % at 500 °C and ~70 % at 700 °C.

ARTICLE INFO

Keywords:
Fluidized bed reactors
Iron oxide reduction
Micron-sized particles
Hydrogen

ABSTRACT

The aim of this study is to investigate the reduction behavior of Fe_2O_3 particles with initially high porosity in a fluidized bed reactor using hydrogen. The powder used is characterized by a large specific surface area and a highly porous initial morphology. The generic Fe_2O_3 powder exhibits a particle structure similar to those typically observed after multiple oxidation/reduction cycles.

The reduction behavior of these Fe_2O_3 particles was studied at temperatures ranging from 500 °C to 700 °C with reduction times of 30 min to 120 min. Physisorption measurements using the Brunauer-Emmett-Teller (BET) method were performed to assess changes in specific surface area before and after reduction. Scanning electron microscopy (SEM) was employed to examine morphological transformations both at the surface and within the particle surface areas by visualizing cross-sections, as well as particle agglomeration. Statistical analysis of the cross-sectional SEM micrographs was performed to determine the pore size growth during the reduction process. Thermogravimetric analysis (TGA) was used together with calorimetry to monitor the reduction degree. Additionally, Mössbauer spectroscopy (MS) and X-ray diffraction (XRD) were used to analyze the contributions of residual oxides after reduction.

The reduction of highly porous Fe_2O_3 in a fluidized bed exhibits temperature- and time-dependent behavior, with the formation of bimodal pore size distributions, a decrease in specific surface area, and reduction degrees exceeding 90 % after 120 min, reaching up to 99.5 % at 700 °C, confirmed through TGA, calorimetry, XRD, and MS, which also revealed minor residual oxides and nano-structured domains at lower temperatures.

* Corresponding author.
Email address: bjoern.stelzner@kit.edu (B. Stelzner).

https://doi.org/10.1016/j.fuel.2025.136422
Received 28 February 2025; Received in revised form 29 July 2025; Accepted 30 July 2025
Available online 13 August 2025

1. Introduction

The transition to sustainable energy systems requires innovative approaches to energy storage and conversion. One promising concept is the iron–iron oxide redox cycle, which enables energy storage and release through reversible oxidation and reduction reactions [1]. In this cycle, iron is oxidized to iron oxide, releasing energy, and later reduced back to iron, enabling a closed-loop system for energy utilization. The potential to perform large-scale oxidation within retrofitted coal power plants makes this process highly attractive [2]. However, efficient reduction of iron oxide to iron remains a critical challenge that dictates the overall feasibility of the system. A fully carbon-free cycle could be achieved using only renewable energy sources for the reduction process [3], which is essential to minimize energy losses and maintain recyclability. Various reduction methods, including hydrogen-based reduction and carbon-assisted pathways, are being explored to optimize efficiency and sustainability [4].

One key issue in this process is the difficulty of fluidizing iron oxide particles at high temperatures. Small micron-sized particles are classified as Geldart group C powders, with strong interparticle forces [5]. This classification indicates that the forces between the particles can be greater than the ability of the fluid to exert a force on the particles. Small particle sizes can result in strong electrostatic charging, hindering fluidization [6], while elevated temperatures further accelerate the defluidization process [6,7]. However, adding nano-sized particles can overcome these forces and enhance fluidization [8]. Also higher gas velocities in reduction experiments intensify hydrodynamic interactions, break up the agglomerates and can thus delay defluidization [9]. Agglomeration and aggregation due to sintering bridges decrease reduction efficiency by limiting gas transport. Temperatures above 500 °C can cause particle aggregation [10]. Surface diffusion results in the formation of sintering necks, which can alter the particle morphology and impact the reduction process, potentially leading to defluidization [11]. The sintering behavior of combusted iron powder was investigated in a packed bed reactor in [12]. Sintering was observed to begin at 575 °C in a nitrogen atmosphere and at 600 °C in hydrogen.

A second critical aspect of this process cycle is the significant impact of oxidation and especially reduction on particle morphology, which affects not only the surface [13] but also the internal structure [14], typically leading to the formation of highly porous architectures throughout the particles. Furthermore, the reduction temperature plays a pivotal role in determining the final surface structure. Higher temperatures generally lead to rougher surfaces with larger pores, which can, in turn, promote agglomeration [9].

The influence of microstructure on the hydrogen-based reduction of iron ore pellets was investigated in [15]. After two hours of reduction at 700 °C, a highly porous iron compound was formed. The observed porosity ranges from approximately 30 % to 45 %. The findings were well aligned with the expected volume loss of about 42 vol.% that occurs during the reduction of FeO to pure iron. It was observed that this reduction step results in the formation of a dense network of pores both internally and on the surface.

The cyclability of the iron/iron oxide was investigated in a fixed-bed reactor by Ref. [16]. SEM micrographs revealed that cyclic oxidation and reduction cause significant changes in surface morphology. Initially, the particles exhibit a smooth surface with no visible nano- and micron-sized pores. After one cycle, the surface becomes rougher, and nano-sized pores emerge, indicating the formation of a sponge-like structure. After eight cycles, particles with open micron-sized structures, resembling cenospheres, were observed in the samples.

Similar observations, such as the formation of nano- and micron-sized pores [12] or even larger micron-sized percolating cavities [14] were reported during the hydrogen-based reduction of iron oxide in a packed bed reactor and in a fluidized bed reactor [9] after a single reduction experiment. However, cenospherical particles have also been observed both after the reduction process in previous studies [9,12] and in the raw material itself [6], making it difficult to conclusively determine whether they originate from the reduction process or were initially present.

Throughout three combustion/reduction cycles, particles exhibit diverse shapes, surface textures, porosities, and internal structures. Nevertheless, the effective conversion and particle size distribution (PSD) remain constant [7].

This study aims to explore the impact of the initial morphology of Fe_2O_3 particles, similar to those formed through multiple oxidation–reduction cycles, on their reduction to iron. To achieve this, a generic Fe_2O_3 powder with a morphology comparable to that reported in the literature [9,12–18] was analyzed. The powder exhibits high initial porosity and the presence of cenosphere-like particles, resulting in a significantly large specific surface area.

2. Reduction of iron oxide

The reduction of Fe_2O_3 can proceed as either a two-step or three-step process, depending on the reaction conditions. As illustrated in the Fe-O phase diagram (Fig. 1), the reduction mechanism is highly temperature-dependent. Below 570 °C, the reduction occurs in two stages: hematite (Fe_2O_3) is first reduced to magnetite (Fe_3O_4) (Eq. 1) and then directly to metallic iron (Fe) (Eq. (2)). Complete reduction of hematite to pure iron can even occur at temperatures as low as 380 °C [19]. Above 570 °C, an additional intermediate step is observed, where magnetite is further reduced to wüstite (FeO) (Eq. 3) before reaching metallic iron (Eq. (4)) [4,20,21]. The reaction enthalpies of formation presented in Eq. (1) to Eq. (4) were calculated using thermodynamic data from Ref. [22]. The Baur–Glässner diagram, which illustrates the equilibrium state of the Fe–O–H system as function of the gas oxidation degree, is shown in Fig. 2.

Temperature plays a critical role in the reduction kinetics. While higher temperatures generally accelerate the initial reduction steps, the final reduction degree tends to be higher at temperatures below 570 °C compared to reactions occurring above 570 °C. This is attributed to more favorable reaction kinetics in the two-step process at lower temperatures [16]. The initial reaction rate for the reduction of iron oxides is strongly influenced by the initial morphology. Higher porosity increases the reactive surface area, thereby accelerating the reduction rate [16,18,23–27]. For instance, Doherty et al. [24] describe the reduction of hematite to magnetite and subsequently to wüstite, emphasizing that significant structural changes may occur during the process.

Ma et al. [28] reported that, during the reduction of hematite pellets, the encapsulation of wüstite islands by iron hindered the outbound diffusion of oxygen in both the core and near-surface

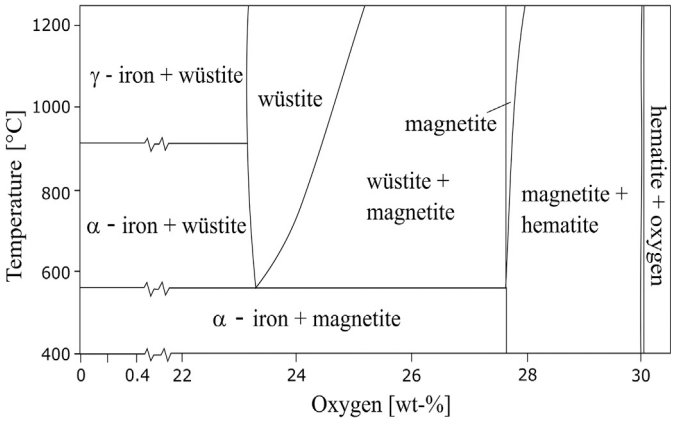

Fig. 1. Fe-O phase diagram based on ref. [29].

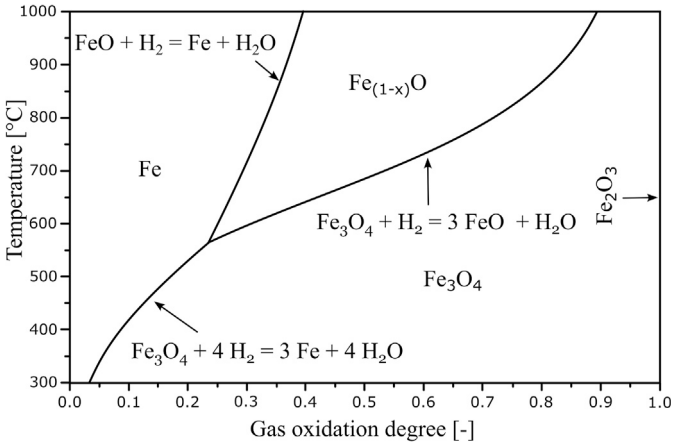

Fig. 2. Baur–Glässner diagram for the Fe–O–H system based on ref. [4].

regions. The subsequently limited presence of lattice defects reduced oxygen transport, thereby impeding uniform and rapid reduction kinetics.

Additionally, Piotrowski et al. [25] reported a transition in the reduction mechanism from being surface-controlled to diffusion-controlled as a thin layer of lower iron oxides forms on the particle surface. In this context, they observed that increasing the hydrogen content in the inlet gas can enhance the reaction rate, underscoring the importance of carefully controlling hydrogen concentration to optimize the reduction process.

$$3\,Fe_2O_3 + H_2 \rightarrow 2\,Fe_3O_4 + H_2O \qquad \Delta_r H^\circ = -7.1\,kJ/mol \qquad (1)$$

$$Fe_3O_4 + 4\,H_2 \rightarrow 3\,Fe + 4\,H_2O \qquad \Delta_r H^\circ = 153.6\,kJ/mol \qquad (2)$$

$$Fe_3O_4 + H_2 \rightarrow 3\,FeO + H_2O \qquad \Delta_r H^\circ = 63.0\,kJ/mol \qquad (3)$$

$$FeO + H_2 \rightarrow Fe + H_2O \qquad \Delta_r H^\circ = 30.2\,kJ/mol \qquad (4)$$

In conclusion, the reduction of iron oxides is a multifaceted, temperature-dependent process characterized by notable changes in reaction mechanisms, surface area, and particle porosity. A comprehensive understanding of the interplay between temperature, gas composition, and particle morphology is crucial for optimizing the reduction process.

3. Experimental setup

3.1. Fluidized bed reactor

The experimental setup is illustrated in Fig. 3. The reactor features an inner diameter of 107 mm and a height of 345 mm. Two fine meshes with a pore size of 15 µm are positioned between the conical and cylindrical sections to induce a pressure drop and ensure uniform flow distribution. The reactor is housed within a retort furnace capable of heating up to 1000 °C. A type-N thermocouple is installed inside the reactor to continuously monitor the gas temperature within the fluidized bed. Prior to the introduction of the powder, the furnace was heated under a nitrogen atmosphere to achieve isothermal conditions. Subsequently, hydrogen was added, and the system was allowed to stabilize again at isothermal conditions. Once the target temperature was reached, the Fe_2O_3 powder was added to the reactor. This setup ensures controlled heating and accurate monitoring of conditions within the fluidized bed. After the reduction time, the fluidized bed was cooled down with pure nitrogen flow to prevent sintering effects.

The nitrogen and hydrogen flows were precisely controlled using thermal mass flow controllers (Bronkhorst B.V.). The pressure drop across the fluidized bed was monitored using a differential pressure sensor (Halstrup-Walcher GmbH, $\Delta p \pm$ 10 kPa). Figure S1 shows the pressure drop curve for the 120 min experiment at 700 °C, representing a worst-case scenario for fluidization behavior.

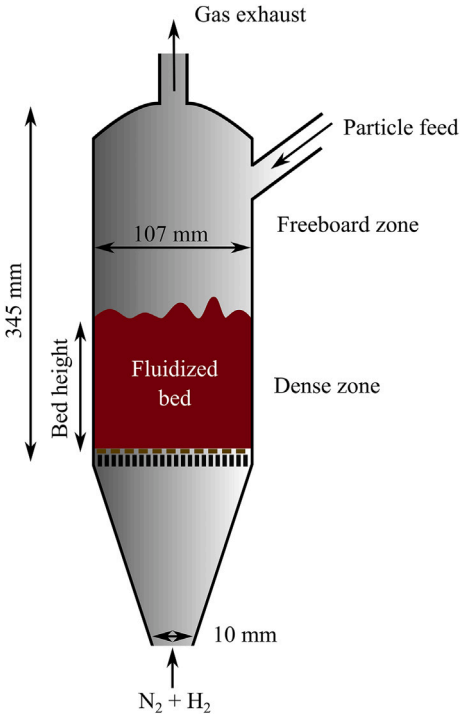

Fig. 3. Schematic sketch of the reactor used in this study.

3.2. Fe_2O_3 powder

The current work focuses on the reduction and characterization of initially highly porous Fe_2O_3 subjected to a single reduction process step, using particles that resemble those typically observed after multiple oxidation/reduction cycles. According to the manufacturer's specifications, the Fe_2O_3 had a stated purity above 97 %. The powder exhibited a diameter of $d_{50} \approx 70$ µm.

Fig. 4 presents SEM micrographs of the surface and cross-sections, illustrating the initially highly porous structure of the Fe_2O_3 particles. The images show two typical particle types: (a) closed particles and (b) cenospherical particles. Additionally, two typical cross-sections are presented: (c) exhibits a highly porous structure with micron-sized voids, whereas (d) shows a denser structure while still displaying cenospherical characteristics. These cenospherical particles, which resemble the structure presented in Fig. 4(b), are well-suited to simulate the morphology typically observed after multiple oxidation/reduction cycles. The particle size distribution (PSD) of the iron oxide powder was measured using laser diffraction (HELOS (H0309) and QUIXEL, Sympatec GmbH). A more detailed description can be found in [30]. The PSD of the initial powder after removing nano-sized particles is presented in Fig. 5.

3.3. Boundary conditions

The reduction experiments were carried out at three different temperatures of 500 °C, 600 °C, and 700 °C. Based on reduction experiments in a fluidized bed reactor and fixed bed conducted by Spreitzer et al. [31] and Hessels et al. [10], respectively, who documented reaction times reaching more than 100 min, the maximum reaction time of 120 min was selected to ensure complete reduction of the samples. To follow the progress in reduction, reaction times of 60 min and 30 min were chosen. A 50/50 mixture by volume of H_2/N_2 was used. Throughout this range of operating conditions, no defluidization was observed, as confirmed by the differential pressure drop across the fluidized bed. Minimum fluidization velocities were calculated using three different correlations: Wen & Yu, Baeyens, and Ergun, as summarized by Werther in Ullmann's Encyclopedia of Industrial Chemistry [32]. However, it has been shown

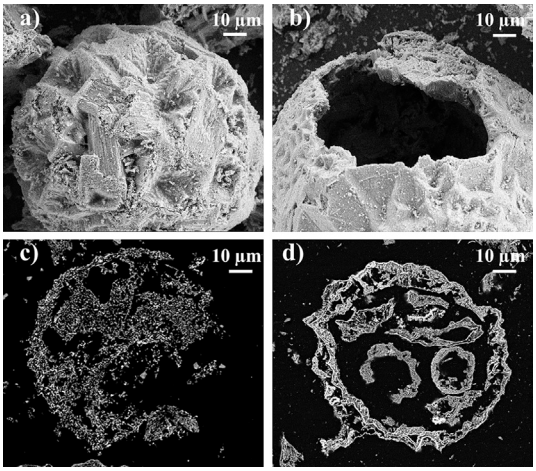

Fig. 4. SEM micrographs of (a) solid Fe_2O_3 particle, (b) cenospherical Fe_2O_3 particle, (c) cross-section of a dense particle, (d) cross-section of a porous particle used in this study.

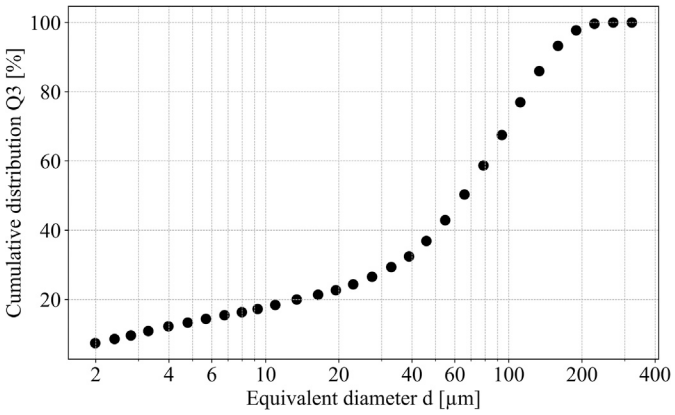

Fig. 5. Particle size distribution of the initial Fe_2O_3 powder before the reduction experiments determined by laser diffraction.

that the minimum fluidization velocity predicted by the Ergun correlation begins to deviate significantly at temperatures exceeding 560 K [13]. The selected inlet velocity of 8.2 cm/s was chosen based on the minimum fluidization velocity across all experiments while ensuring a maximum limit to prevent particle discharge from the reactor. Thus, the multiples of the minimum fluidization velocity varied between 16 and 18. Before the reduction experiments, the powder was fluidized in a cold reactor at a comparable fluidization rate for 120 min to remove particles in the nano-size range and to avoid significant material loss during the reduction. Furthermore, a cyclone separator with a separation efficiency of about 1 µm was installed downstream of the reactor. In all experiments, no significant material losses were observed.

3.4. Applied measurement techniques

The particle surface was visualized using a LEO 1530 Gemini with a Schottky field emitter. Subsequent backscattered electron imaging was performed using an EI Quanta 650 ESEM, also equipped with a Schottky field emitter. The acceleration voltages applied for the investigations ranged from 10 kV to 20 kV. The sample chamber was evacuated to a pressure of approximately $p \approx 10^{-4}$ Pa using vacuum pumps. To reveal the internal structure of the particles, selected samples were embedded in resin and polished for a cross-sectional analysis.

The pore structure was statistically analyzed for each boundary condition using the cross-sectional micrographs. For each investigated particle, the analysis was conducted at two magnifications to resolve both nano-sized and micron-sized pore structures. The micrographs were binarized using a threshold set at 50 % of the grayscale range (from minimum to maximum intensity). Subsequently, noise was removed through a non-linear digital image processing technique. For that, a median filter of 3 pixels followed by two times numerical erode and dilate steps was used to remove small features and edge effects during detection. The resulting resolution was 20 nm at magnification 10kx and 135 nm at magnification 2.5kx.

A BELSORP-mini (BEL-Japan Inc.) was used for physisorption measurements (Brunauer-Emmett-Teller, BET). The device recorded nitrogen adsorption and desorption using manometric and volumetric measurement techniques. First, the samples were weighed and placed into measurement cells, which were then evacuated using a vacuum pump. A sample mass of approximately 500 ± 50 mg was used for each measurement. Nitrogen adsorption was subsequently carried out at 77 K (−196 °C). Each data point presented in this study is based on three independent measurements to ensure reliability.

Thermogravimetric analysis (TGA) was employed to determine the reduction degree. Isothermal measurements were conducted with a TG 209 F1 Libra (Netzsch Gerätebau GmbH, Germany) at temperatures of 500 °C, 600 °C, and 700 °C. The samples weighed around 5 ± 0.3 mg. Following sample insertion, the TGA was heated at a rate of 20 K/min under an inert nitrogen atmosphere. Once thermal equilibrium was achieved, the gas flow was switched to an N_2/H_2 mixture (90/10 vol.%) to initiate the reduction experiments. A reaction time of 5 hours was chosen to ensure full reduction of the samples. The TGA was temperature-calibrated using the melting points of In, Sn, Bi, Zn, Al, and Ag as reference materials.

Calorimetric measurements were performed using an IKA C200 calorimeter to accurately determine the reduction degree of the reduced powder. Before the experiments, the calorimeter was calibrated with benzoic acid of known calorific value and verified with defined mixtures of iron and iron oxide. The sample (approximately 0.3 g) is placed in a vessel pressurized with oxygen. After controlled ignition, the specific calorific value is determined by assuming complete combustion/oxidation and measuring the resulting temperature increase (ΔT) of the calorimeter system, based on the known sample mass. The experimental results show an excellent linear correlation with the theoretical values, achieving a regression coefficient of $R^2 = 0.998$. Additionally, masses were measured using a high-precision scale (SI-234, Denver Instrument) to further enhance calibration accuracy. These measurements also demonstrated a strong linear correlation, with a regression coefficient of $R^2 = 0.957$, ensuring high reliability of the reduction degree determination.

^{57}Fe Mössbauer spectroscopy is performed at room temperature with a home-built setup – a velocity drive unit from Halder Instruments, a proportional counter as detector, a preamplifier, an amplifier and a CMCA-500 (Wissel) for discrimination and data collection. The ^{57}Co/Rh source had an initial activity of 100 mCi and is moved in a triangular waveform. A 25 µm α-iron foil is used as calibration standard. Samples were carefully ground in an agate mortar prior to the measurements. Sample loadings were in the range of 15–22 mg cm^{-2}. Fitting of the experimental data is performed with the SYNCmoss software package [33] using Pseudo-Voigt line shapes. In the fits of the samples that indicated only a low abundance of Fe_3O_4 or α-Fe_2O_3, their hyperfine interaction parameters were fixed to those commonly found for the respective oxides [34,35]. Composition calculations were performed according to [36], using Lamb-Mössbauer factors summarized in [37]. Further information on samples and parameters is provided in the ESI.

Powder diffractograms were recorded with a PANalytical X'pert Pro diffractometer using Cu-Kα radiation (Cu-K-α1 = 1.5406 Å) and a Ni filter. The diffractograms were recorded with a step size of 0.017° and 2Θ ranging from 5–80° (0.53 s acquisition time per data point). The

obtained reflections were compared to reference data sets available in the Inorganic Crystal Structure Database (ICSD) [38].

4. Results and discussion

4.1. Impact on morphology

Fig. 6 presents secondary electron micrographs of the surface and corresponding backscattered electron micrographs of the cross-section at 500 °C, 600 °C, and 700 °C after 120 min of reduction. Images are shown at two different magnifications to highlight both surface morphology and internal structural changes.

All surfaces exhibit a high density of nano-sized pores and micro-scale voids. However, larger voids inside the particles are observed both after reduction and in the raw material (see Fig. 4), making their origin difficult to determine. Therefore, a statistical analysis of the cross-sectional SEM micrographs was carried out to reveal structural changes after reduction, and the resulting circular pore size distributions are presented in Fig. 7.

The data reveal a bimodal pore size distribution: a substantial fraction of smaller pores, with a mean diameter of approximately 150 nm, is already present in the initial powder. After the reduction process, a decline in the first mode and a pronounced increase in the second mode are observed, indicating the formation and growth of larger pores. In this second mode, circular pore diameters start at around 500 nm and progressively increase in size. The increase in micron-sized pores during reduction was also observed by Ma et al. [39]. However, the statistical analysis does not capture very large voids due to their rare, single-event nature and does not allow for a robust quantitative assessment of temperature effects on the development of large-scale pores. While cross-sectional SEM micrographs offer valuable insight into pore morphology, they do not capture information about the third dimension, making it challenging to distinguish between open and closed porosity or to determine whether pores form isolated voids or interconnected channels. A representative fully post-processed SEM micrograph is available in the supplementary material (Fig. S2).

The specific surface areas of the initial and reduced samples at different temperatures are presented in Fig. 8. For the initial Fe_2O_3 powder, a specific surface area of $a_s = 3.98\ m^2/g$ was measured. The specific surface area decreases significantly with increasing temperature. These findings align with the SEM micrographs, which reveal that the reduction process generates larger micron-sized pores, potentially decreasing the specific surface area. At 500 °C, only a marginal reduction of approximately 15 % is observed, whereas at 700 °C, it drops by nearly 70 %. At this higher temperature, the duration of exposure has no noticeable impact on the surface area. However, at 500 °C, a more pronounced difference is observed, indicating that exposure time plays a more critical role at lower temperatures.

4.2. Reduction degree

The reduction degree RD in relation to Fe_2O_3 can be used to quantify the progress of the reaction:

$$RD = \frac{m_{Fe_2O_3,0} - m(t)}{m_{Fe_2O_3,0} - m_{Fe}} \tag{5}$$

where $m(t)$ is the measured mass at time t, $m_{Fe_2O_3,0}$ is the initial mass of Fe_2O_3 and m_{Fe} is the corresponding mass when iron species are completely reduced to iron. Fig. 9 shows typical progression of RD as a function of reaction time during thermogravimetric analysis at varying temperatures. The total mass loss corresponds to pure Fe_2O_3, confirming its high purity. As expected, the reduction time increases significantly with decreasing temperature. It has been reported in [18] that the initial reaction rate is temperature-dependent. However, at temperatures above 570 °C, the reduction pathway from Fe_3O_4 to FeO and subsequently to metallic iron (Eqs. 3 and 4) becomes transport-limited once a critical layer of FeO and metallic Fe has formed [40] and remaining FeO islands were encapsulated by iron, inhibiting oxygen diffusion [28]. In contrast, at lower temperatures, the direct reduction from Fe_3O_4 to metallic iron (Eq. 2) can be faster over extended periods. This effect is not observed in highly porous initial particles, likely because their porosity prevents the formation of a significant FeO layer, thereby mitigating transport limitations.

A comparison of the reduction degree determined using a calorimeter and TGA is shown in Fig. 10. In preliminary experiments for verification, defined mixtures of pure iron and Fe_2O_3 were prepared and subsequently oxidized using calorimetry and reduced using TGA method.

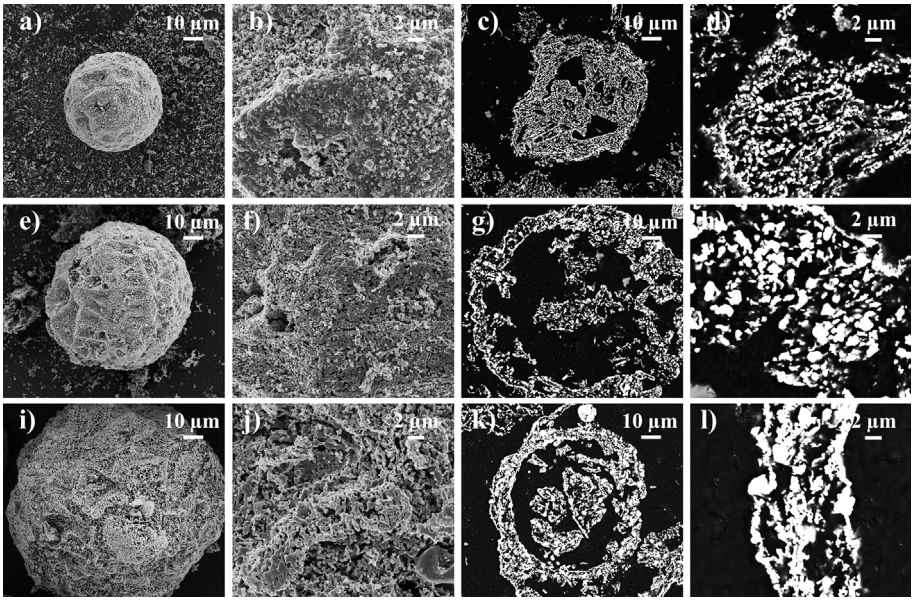

Fig. 6. From left to right: (a) SEM micrographs of the particle surfaces, (b) surface at increased magnification, (c) corresponding cross sectional analysis by backscattered electrons micrographs, and (d) cross section at higher magnification for different processing temperatures at 120 min reduction time: (a)–(d) 500 °C, (e)–(h) 600 °C and (i)–(l) 700 °C.

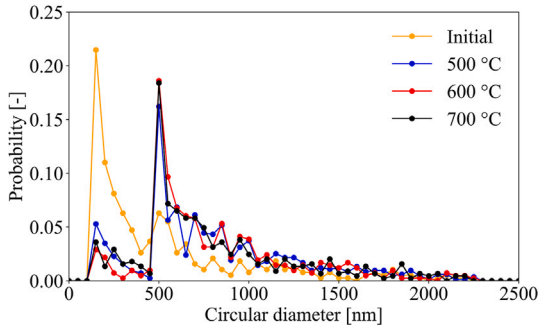

Fig. 7. Distribution of the circular pore size diameter of the initial and reduced powder after 120 min.

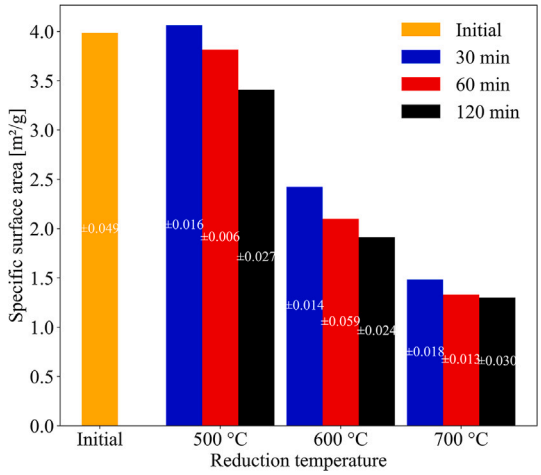

Fig. 8. Specific surface area of the initial sample and samples after reduction at different temperatures and reduction times.

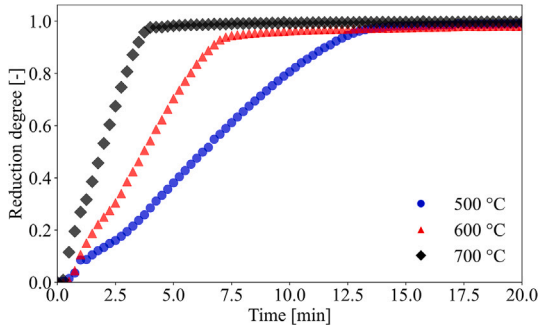

Fig. 9. Thermogravimetric data showing the reduction degree of Fe_2O_3 at temperatures ranging from 500 °C to 700 °C in a N_2/H_2 gas mixture (90/10 vol.%), starting from t = 0 min.

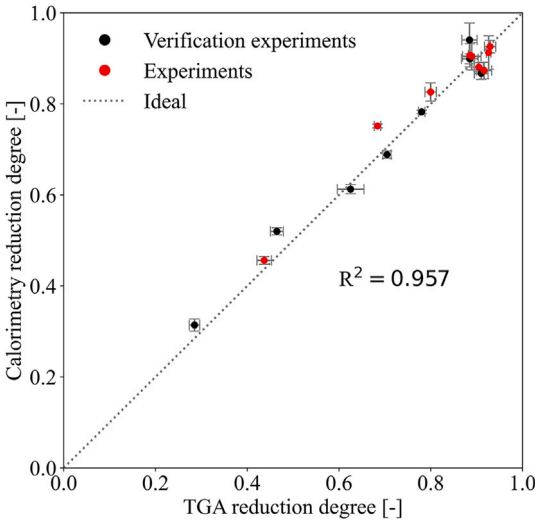

Fig. 10. Comparison of the reduction degree using thermogravimetric analysis (TGA) and calorimetry.

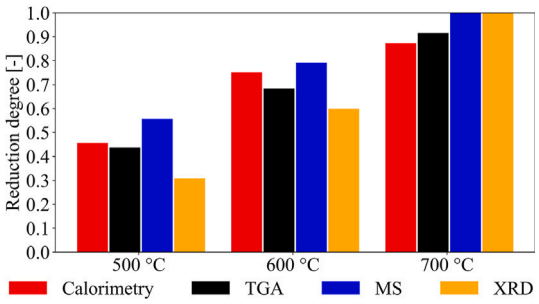

Fig. 11. Comparison of the reduction degree after 30 min of reduction measured by calorimetry, TGA, MS, and XRD.

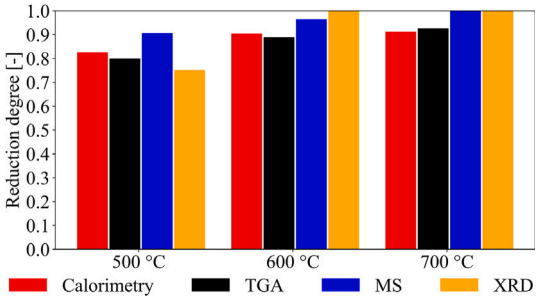

Fig. 12. Comparison of the reduction degree after 60 min of reduction measured by calorimetry, TGA, MS, and XRD.

The results demonstrate strong agreement, even for mixtures containing as little as 30 % iron available for final oxidation. Additionally, all reduction experiments conducted in the fluidized bed reactor are presented. Both measurement techniques, particularly the calorimeter, have proven to be reliable and cost-effective tools for accurately determining reduction degrees.

The results are presented in Figs. 11–13 for reduction times of 30 min, 60 min, and 120 min, respectively. The reduction degree is correlated with the reduction temperature and compared with data obtained from MS and XRD measurements. At a reduction time of 30 min, the degree of reduction at 500 °C remained below 50 %, while at 600 °C it reached approximately 70 %. At 700 °C, near-complete reduction was achieved, with calorimetry and TGA indicating reduction degrees around 90 %, and XRD and MS indicating high conversion to metallic iron, with no resolvable oxide phases in either the MS spectra or XRD diffractograms. After 120 min, the maximum reduction degree at 500 °C approached 90 %, indicating that longer reduction times can compensate for the slower kinetics at lower temperatures. At 600 °C, the reaction rate noticeably slowed between 60 min and 120 min, consistent with findings reported by Ma et al. [28], suggesting transport limitations due to encapsulation of intermediate FeO phase. Across all experiments, a consistently high reduction degree exceeding 90 % was observed after 120 min, regardless of the measurement technique, demonstrating the

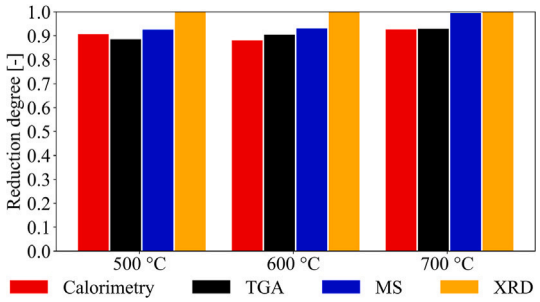

Fig. 13. Comparison of the reduction degree after 120 min of reduction measured by calorimetry, TGA, MS, and XRD.

effectiveness of prolonged reduction times at elevated temperatures. In general, good agreement was observed between calorimetry and TGA results. A tendency toward slightly higher reduction degrees was noted with MS, while XRD consistently reported slightly lower values.

The iron-related composition was measured by XRD and MS to enable the determination of residual iron oxide species and estimate the degree of reduction. The results obtained after 30 min, 60 min and 120 min are given in Figs. 14–16, respectively. It should be noted that the ordinate axis is not uniformly scaled in order to enhance readability.

After 30 min of reduction, Fe_2O_3 is nearly completely converted across all tested temperatures, with only MS detecting minor residual fractions. At 500 °C, the one-step reaction from Fe_3O_4 to Fe can be observed. At 600 °C, FeO is clearly observed as an intermediate phase, demonstrating a stepwise reduction pathway from Fe_2O_3 to Fe via Fe_3O_4 and FeO. In contrast, at 700 °C, the reduction proceeds more rapidly, resulting in full conversion to metallic iron within a time frame of 30 min.

When the reduction time is extended to 60 min, the degree of reduction continues to progress at 500 °C, with Fe_3O_4 identified as the primary residual oxide. At 600 °C, the material is nearly fully reduced; only MS detects trace amounts of residual oxides close to the detection limit, indicating near-complete conversion. After 120 min of reduction, residual iron oxides are detectable only by MS, suggesting an almost complete reduction. Overall, the data show that higher temperatures and longer reduction times lead to more complete conversion to metallic iron.

This indicates that it is beneficial to combine various analytical methods that follow different physical principles (XRD: constructive interference patterns at crystallographic planes versus nuclear resonance absorption in case of MS). The combination of XRD and MS, improves the

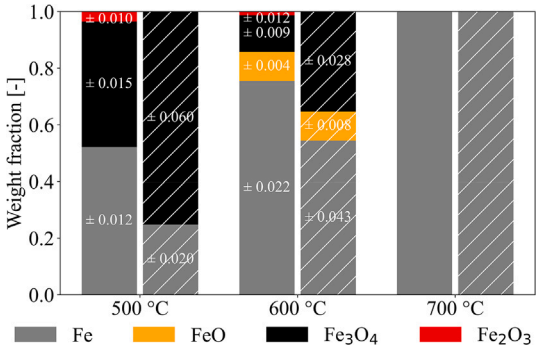

Fig. 14. Weight fraction of the residual iron oxides after 30 min of reduction at different temperatures, measured by Mössbauer spectroscopy (MS) and X-ray diffraction (XRD). Continuous bars indicate MS, while dashed bars represent XRD.

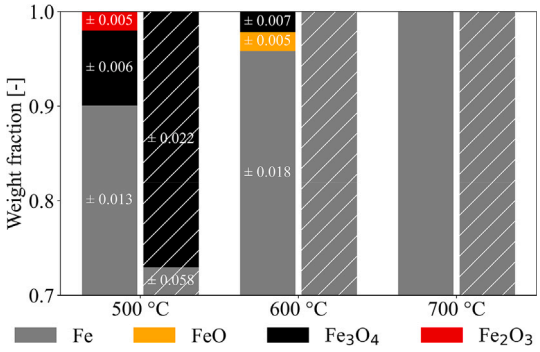

Fig. 15. Weight fraction of the residual iron oxides after 60 min of reduction at different temperatures, measured by Mössbauer spectroscopy (MS) and X-ray diffraction (XRD). Continuous bars indicate MS, while dashed bars represent XRD.

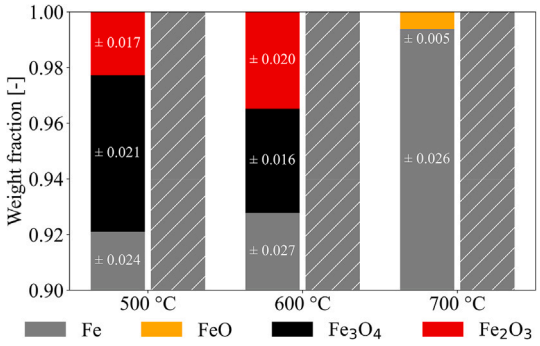

Fig. 16. Weight fraction of the residual iron oxides after 120 min of reduction at different temperatures, measured by Mössbauer spectroscopy (MS) and X-ray diffraction (XRD). Continuous bars indicate MS, while dashed bars represent XRD.

trust level in the assignment of intermediate species within the reduction process [40], while differences might indicate changing sensitivity to amorphous parts of the sample.

All diffractograms and MS spectra, along with key boundary conditions, are provided as Figure S3, Figure S4 and Table S1 in the supplementary material.

5. Conclusion

This study investigates the reduction of Fe_2O_3 in a fluidized bed with a particle system representative of those subjected to multiple oxidation–reduction cycles. The experiments were conducted at temperatures ranging from 500 °C to 700 °C, resulting in two distinct reduction pathways: direct reduction from Fe_3O_4 to Fe and a stepwise reduction from Fe_3O_4 to FeO before forming metallic Fe.

The reduction of initial highly porous Fe_2O_3 particles results in the formation of micron-sized pores both on the surface and within the particle. The statistical analysis of cross-sectional SEM micrographs reveals a bimodal pore size distribution, showing a shift from predominantly smaller pores in the initial powder to a second mode with larger pores after reduction. As a result, the specific surface area decreases. The reduction degree at 120 min exceeds 90 % across all reduction temperatures and measurement techniques. With decreasing reduction time, the reduction degree drops to 70 % at 500 °C after 30 min. TGA and calorimetry have been demonstrated to be fast and reliable methods for determining the reduction degree.

In conclusion, Mössbauer spectroscopy revealed temperature-dependent reduction behavior. At 500 °C and 600 °C, a reduction degree

of around 94 % was achieved, with residual Fe_3O_4 and Fe_2O_3. The highest reduction degree of 99.5 % occurred at 700 °C, leaving only FeO. Mössbauer spectroscopy detected minor oxide signals near the detection limit, with possible contributions from amorphous phases. Higher temperatures reduced the contribution of the broader α-Fe sextet, indicating fewer nano-structured domains.

Lower reduction times were analyzed using XRD: after 60 min of reduction, a high reduction degree was achieved, with 94.4 % metallic iron at 500 °C and full conversion at 600 °C. After 30 min, the reduction degree was lower, with 68 % metallic iron at 500 °C and 84 % at 600 °C. These results indicate that longer reduction times and higher temperatures lead to better reduction.

CRediT authorship contribution statement

Malte Seitz: Writing – original draft, Visualization, Investigation. **Martin P. Kannengießer:** Writing – original draft, Visualization, Investigation. **Björn Stelzner:** Writing – original draft, Supervision, Project administration, Conceptualization. **Fabian P. Hagen:** Writing – review & editing, Supervision, Project administration, Conceptualization. **Lukas Braun:** Writing – review & editing, Investigation. **Jonas Kaltenbach:** Writing – review & editing, Investigation. **Kerstin Märkle:** Writing – review & editing, Investigation. **Martin Peterlechner:** Writing – review & editing, Investigation, Formal analysis. **Jonas Spielmann:** Writing – review & editing, Investigation. **Dmitry E. Doronkin:** Writing – review & editing, Supervision, Project administration. **Max P. Deutschmann:** Writing – review & editing, Investigation. **Jan-Dierk Grunwaldt:** Writing – review & editing, Supervision, Project administration, Funding acquisition. **Yolita M. Eggeler:** Writing – review & editing, Supervision, Project administration, Funding acquisition. **Ulrike I. Kramm:** Writing – review & editing, Supervision, Project administration, Funding acquisition. **Hermann Nirschl:** Writing – review & editing, Supervision, Project administration, Funding acquisition. **Dimosthenis Trimis:** Writing – review & editing, Supervision, Project administration, Funding acquisition, Conceptualization.

Declaration of competing interest

The authors declare that they have no known competing financial interests or personal relationships that could have appeared to influence the work reported in this paper.

Acknowledgments

This research contributes to the MTET program on Resource and Energy Efficiency within the Anthropogenic Carbon Cycle (38.05.01) and Power-based Fuels and Chemicals (38.03.02) of the Helmholtz Association. It was conducted as part of the Clean Circles cluster project. The authors gratefully acknowledge financial support from the Strategy Funds of the KIT Presidium, the German Research Foundation (project no.: 558715615), and the Friedrich and Elisabeth Boysen Foundation (BOY-200).

Appendix A. Supplementary data

Supplementary data for this article can be found online at doi:10.1016/j.fuel.2025.136422.

Data availability

Data will be made available on request.

References

[1] Bergthorson JM, Goroshin S, Soo MJ, Julien P, Palecka J, Frost DL, et al. Direct combustion of recyclable metal fuels for zero-carbon heat and power. Appl Energy 2015;160:368–82. https://doi.org/10.1016/j.apenergy.2015.09.037. https://www.sciencedirect.com/science/article/pii/S0306261915011071

[2] Janicka J, Debiagi P, Scholtissek A, Dreizler A, Epple B, Pawellek R, et al. The potential of retrofitting existing coal power plants: a case study for operation with green iron. Appl Energy 2023;339:120950. https://doi.org/10.1016/j.apenergy.2023.120950. https://www.sciencedirect.com/science/article/pii/S0306261923003148

[3] Julien P, Bergthorson JM. Enabling the metal fuel economy: green recycling of metal fuels. Sustain Energy Fuels 2017;1:615–25. https://doi.org/10.1039/C7SE00004A. http://dx.doi.org/10.1039/C7SE00004A

[4] Spreitzer D, Schenk J. Reduction of iron oxides with hydrogen—a review. Steel Res Int 2019;90(10):1900108. https://doi.org/10.1002/srin.201900108. https://onlinelibrary.wiley.com/doi/pdf/10.1002/srin.201900108

[5] Geldart D. Types of gas fluidization. Powder Technol 1973;7(5):285–92. https://doi.org/10.1016/0032-5910(73)80037-3. https://www.sciencedirect.com/science/article/pii/0032591073800373

[6] Liu X, Zhang X, Li J, Zhu Q, Deen NG, Tang Y. Regeneration of iron fuel in fluidized beds, Part I: defluidization experiments and theoretical prediction model. Powder Technol 2023;420:118182. https://doi.org/10.1016/j.powtec.2022.118182. https://www.sciencedirect.com/science/article/pii/S0032591022010634

[7] Stevens NC, Prasidha W, Deen NG, Meeuwsen L, Baigmohammadi M, Shoshin Y, et al. Cyclic reduction of combusted iron powder: a study on the material properties and conversion reaction in the iron fuel cycle. Powder Technol 2024;441:119786. https://doi.org/10.1016/j.powtec.2024.119786. https://www.sciencedirect.com/science/article/pii/S0032591024004297

[8] Zhou Y, Zhu J. A review on fluidization of geldart group c powders through nanoparticle modulation. Powder Technol 2021;381:698–720. https://doi.org/10.1016/j.powtec.2020.12.011. https://www.sciencedirect.com/science/article/pii/S0032591020311724

[9] Liu X, Zhang X, Li J, Zhu Q, Deen NG, Tang Y. Regeneration of iron fuel in fluidized beds Part II: reduction experiments. Powder Technol 2023;420:118183. https://doi.org/10.1016/j.powtec.2022.118183. https://www.sciencedirect.com/science/article/pii/S0032591022010646

[10] Hessels CJM, Homan TAM, Deen NG, Tang Y. Reduction kinetics of combusted iron powder using hydrogen. Powder Technol 2022;407:117540. https://doi.org/10.1016/j.powtec.2022.117540. https://www.sciencedirect.com/science/article/pii/S003259102200434X

[11] Knight PC, Seville JPK, Kamiya H, Horio M. Modelling of sintering of iron particles in high-temperature gas fluidisation. Chem Eng Sci 2000;55(20):4783–87. https://doi.org/10.1016/S0009-2509(00)00055-5. https://www.sciencedirect.com/science/article/pii/S0009250900000555

[12] Hessels CJM, Smeets AHJ, Finotello G, Deen NG, Tang Y. Sintering behavior of combusted iron powder in a packed bed reactor with nitrogen and hydrogen. Particuology 2023;83:8–17. https://doi.org/10.1016/j.partic.2023.02.007. https://www.sciencedirect.com/science/article/pii/S1674200123000470

[13] Hessels CJM, Lelivelt DWJ, Stevens NC, Tang Y, Deen NG, Finotello G. Minimum fluidization velocity and reduction behavior of combusted iron powder in a fluidized bed. Fuel 2023;342:127710. https://doi.org/10.1016/j.fuel.2023.127710. https://www.sciencedirect.com/science/article/pii/S001623612300323X

[14] Choisez L, Hemke K, Özgün Ö, Pistidda C, Jeppesen H, Raabe D, et al. Hydrogen-based direct reduction of combusted iron powder: deep pre-oxidation, reduction kinetics and microstructural analysis. Acta Mater 2024;268:119752. https://doi.org/10.1016/j.actamat.2024.119752. https://www.sciencedirect.com/science/article/pii/S1359645424001058

[15] Kim S-H, Zhang X, Ma Y, Filho IRS, Schweinar K, Angenendt K, et al. Influence of microstructure and atomic-scale chemistry on the direct reduction of iron ore with hydrogen at 700 °C. Acta Mater 2021;212:116933. https://doi.org/10.1016/j.actamat.2021.116933. https://www.sciencedirect.com/science/article/pii/S135964542100313X

[16] Kuhn C, Kirn M, Tischer S, Deutschmann O. Micron-sized iron particles as energy carrier: cycling experiments in a fixed-bed reactor. Proc Combust Inst 2024 Jan 40(1):105207. https://doi.org/10.1016/j.proci.2024.105207. https://www.sciencedirect.com/science/article/pii/S1540748924000178

[17] Deutschmann MP, Sperling A, Covini E, Böhm B, Dreizler A, Nirschl H. Single iron particle combustion - a morphology study of partially oxidized iron particles. Powder Technol 2024;445:120102. https://doi.org/10.1016/j.powtec.2024.120102. https://www.sciencedirect.com/science/article/pii/S0032591024007460

[18] Kuhn C, Knapp A, Deutschmann MP, Spielmann J, Tischer S, Kramm UI, et al. Iron as recyclable metal fuel: unraveling oxidation behavior and cyclization effects through thermogravimetric analysis, wide-angle X-ray scattering and Mössbauer Spectroscopy. ChemSuschem 2024;17(15):e202400351. https://doi.org/10.1002/cssc.202400351. https://onlinelibrary.wiley.com/doi/abs/10.1002/cssc.202400351

[19] Jozwiak WK, Kaczmarek E, Maniecki TP, Ignaczak W, Maniukiewicz W. Reduction behavior of iron oxides in hydrogen and carbon monoxide atmospheres. Appl Catal A Gen 2007 Jul 326(1):17–27. https://doi.org/10.1016/j.apcata.2007.03.021. https://www.sciencedirect.com/science/article/pii/S0926860X07002062

[20] Heidari A, Niknahad N, Iljana M, Fabritius T. A review on the kinetics of iron ore reduction by hydrogen. Materials 2021;14(24):7540. https://doi.org/10.3390/ma14247540. https://www.mdpi.com/1996-1944/14/24/7540

[21] Hou B, Zhang H, Li H, Zhu Q. Study on kinetics of iron oxide reduction by hydrogen. Chin J Chem Eng 2012;20(1):10–17. https://doi.org/10.1016/S1004-9541(12)60357-7

[22] NIST standard reference database. https://doi.org/10.18434/T42S31, [Accessed: 2025-02-25].

[23] Spielmann J, Braig D, Streck A, Gustmann T, Kuhn C, Reinauer F, et al. Exploring the oxidation behavior of undiluted and diluted iron particles for energy storage: Mössbauer spectroscopic analysis and kinetic modeling. Phys Chem Chem Phys 2024;26(17):13049–60. https://doi.org/10.1039/D3CP03484D. https://pubs.rsc.org/en/content/articlelanding/2024/cp/d3cp03484d

[24] Doherty RD, Hutchings KM, Smith JD, Yörük S. The reduction of hematite to wustite in a laboratory fluidized bed. Metall Trans B 1985 Sep 16(3):425–32. https://doi.org/10.1007/BF02654840.
[25] Piotrowski K, Mondal K, Lorethova H, Stonawski L, Szymański T, Wiltowski T. Effect of gas composition on the kinetics of iron oxide reduction in a hydrogen production process. Int J Hydrogen Energy 2005 Dec 30(15):1543–54. https://doi.org/10.1016/j.ijhydene.2004.10.013. https://www.sciencedirect.com/science/article/pii/S0360319904003428
[26] He J, Li K, Zhang J, Conejo AN. Reduction kinetics of compact hematite with hydrogen from 600 to 1050 °C. Metals 2023 Mar 13(3):464. https://doi.org/10.3390/met13030464. https://www.mdpi.com/2075-4701/13/3/464
[27] Parkinson GS. Iron oxide surfaces. Surf Sci Rep 2016 Mar 71(1):272–365. https://doi.org/10.1016/j.surfrep.2016.02.001. https://www.sciencedirect.com/science/article/pii/S0167572916000054
[28] Ma Y, Filho IRS, Zhang X, Nandy S, Barriobero-Vila P, Requena G, et al. Hydrogen-based direct reduction of iron oxide at 700 °C: heterogeneity at pellet and microstructure scales. Int J Miner Metall Mater 2022;29(10):1901–07. https://doi.org/10.1007/s12613-022-2440-5
[29] Darken LS, Gurry RW. The system iron - oxygen. II. Equilibrium and thermodynamics of liquid oxide and other phases. J Am Chem Soc 1946;68(5):798–816. https://doi.org/10.1021/ja01208a041
[30] Buchheiser S, Deutschmann MP, Rhein F, Allmang A, Fedoryk M, Stelzner B, et al. Particle and phase analysis of combusted iron particles for energy storage and release. Materials 2023;16(5):2009. https://doi.org/10.3390/ma16052009. https://www.mdpi.com/1996-1944/16/5/2009
[31] Spreitzer D, Schenk J. Fluidization behavior and reducibility of iron ore fines during hydrogen-induced fluidized bed reduction. Particuology 2020;52:36–46. https://doi.org/10.1016/j.partic.2019.11.006
[32] Werther J. Fluidized-bed reactors. In: Ullmann's encyclopedia of industrial chemistry. John Wiley & Sons, Ltd; 2007. https://onlinelibrary.wiley.com/doi/pdf/10.1002/14356007.b04_239.pub2, doi:https://doi.org/10.1002/14356007.b04_239.pub2. https://onlinelibrary.wiley.com/doi/abs/10.1002/14356007.b04_239.pub2
[33] Yaroslavtsev S. *SYNCmoss* software package for fitting Mössbauer spectra measured with a synchrotron Mössbauer source. J Synchrotron Radiat 2023;30(3):596–604. https://doi.org/10.1107/S1600577523001686
[34] Greenwood NN, Gibb TC. Mössbauer spectroscopy. Berlin, Heidelberg: Springer; 1971. https://doi.org/10.1007/978-94-009-5697-1
[35] Oh SJ, Cook DC, Townsend HE. Characterization of iron oxides commonly formed as corrosion products on steel. Hyperfine Interact 1998;112(1):59–66. https://doi.org/10.1023/A:1011076308501
[36] Meisel W, Kreysa G. Cheminform abstract: Relative Mössbauer-konstanten von eisenverbindungen zur quantitativen analyse von gemischten. Chem Inf 1984;4(7):689–93. https://doi.org/10.1002/chin.197307494
[37] Spielmann J, Braig D, Streck A, Gustmann T, Kuhn C, Reinauer F, et al. Exploring the oxidation behavior of undiluted and diluted iron particles for energy storage: Mössbauer spectroscopic analysis and kinetic modeling. Phys Chem Chem Phys 2024;26:13049–60. https://doi.org/10.1039/D3CP03484D. http://dx.doi.org/10.1039/D3CP03484D
[38] Inorganic Crystal Structure Database. Inorganic crystal structure database (icsd), 2024, https://icsd.fiz-karlsruhe.de/. [Accessed: 2025-02-20].
[39] Ma Z, Xiao R, Chen L. Redox reaction induced morphology and microstructure evolution of iron oxide in chemical looping process. Energy Convers Manag 2018;168:288–95. https://doi.org/10.1016/j.enconman.2018.05.013. https://www.sciencedirect.com/science/article/pii/S0196890418304825
[40] Braun L, Spielmann J, Doronkin DE, Kuhn C, Maliugin A, Sharapa DI, et al. Following the structural changes of iron oxides during reduction under transient conditions. ChemSuschem 2024;17(24):e202401045. https://doi.org/10.1002/cssc.202401045. https://chemistry-europe.onlinelibrary.wiley.com/doi/pdf/10.1002/cssc.202401045